analytical chemistry

Editors' Highlight

pubs.acs.org/ac

Micro X-ray Fluorescence Imaging in a Tabletop Full Field-X-ray Fluorescence Instrument and in a Full Field-Particle Induced X-ray Emission End Station

Francesco Paolo Romano,*[,†,‡] Claudia Caliri,[‡,§] Luigi Cosentino,[‡] Santo Gammino,[‡] David Mascali,[‡] Lighea Pappalardo,[†,‡] Francesca Rizzo,[‡,§] Oliver Scharf,[∥] and Hellen Cristine Santos[‡]

[†]CNR, Istituto per i Beni Archeologici e Monumentali, Via Biblioteca 4, 95124 Catania, Italy

[‡]INFN, Laboratori Nazionali del Sud, Via Santa Sofia 62, 95123, Catania, Italy

[§]Università di Catania, Dipartimento di Fisica e Astronomia, Via A. Doria 6, 95123, Catania, Italy

[∥]IFG Institute for Scientific Instruments GmbH, Rudower Chaussee 29/31, 12489 Berlin, Germany

Supporting Information

ABSTRACT: A full field-X-ray camera (FF-XRC) was developed for performing the simultaneous mapping of chemical elements with a high lateral resolution. The device is based on a conventional CCD detector coupled to a straight shaped polycapillary. Samples are illuminated at once with a broad primary beam that can consist of X-rays or charged particles in two different analytical setups. The characteristic photons induced in the samples are guided by the polycapillary to the detector allowing the elemental imaging without the need for scanning. A single photon counting detection operated in a multiframe acquisition mode and a processing algorithm developed for event hitting reconstruction have enabled one to use the CCD as a high energy resolution X-ray detector. A novel software with a graphical user interface (GUI) programmed in Matlab allows full control of the device and the real-time imaging with a region-of-interest (ROI) method. At the end of the measurement, the software produces spectra for each of the pixels in the detector allowing the application of a least-squares fitting with external analytical tools. The FF-XRC is very compact and can be installed in different experimental setups. This work shows the potentialities of the instrument in both a full field-micro X-ray fluorescence (FF-MXRF) tabletop device and in a full field-micro particle induced X-ray emission (FF-MPIXE) end-station operated with an external proton beam. Some examples of applications are given as well.

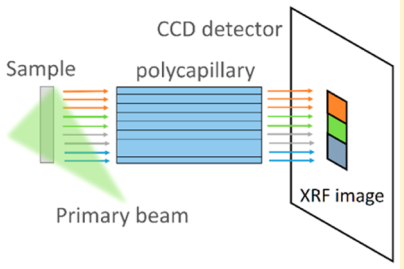

Micro X-ray fluorescence spectroscopy is a well-established method for performing the nondestructive elemental analysis down to the micrometer scale of length. In many analytical applications, the possibility to perform the simultaneous elemental imaging with high lateral resolution and high spectroscopic capabilities is mandatory to obtain straightforward and unambiguous information.[1,2]

Depending on the analytical technique, the X-ray emission can be induced on samples by X-rays or charged particle beams. In the case of micro X-ray fluorescence (MXRF), the primary X-ray beam from a tube or in a synchrotron beamline is focused down the micrometric scale with X-ray optics.[3−5] In the case of micro particle induced X-ray emission (MPIXE), dedicated beamlines in accelerator equipped laboratories are necessary in order to focus the charged particle beam (usually low energy protons) to a dimension of few tens of micrometers or less.[6−9]

Focused beams are then used for scanning samples in order to build-up the elemental maps point-by-point.[10−17]

The scanning approach presents high chemical sensitivity and high spatial resolution. The main limits consist of (i) requirement of a flat geometry for samples under investigation, (ii) a long measurement time when scanning is performed in a wide area with a small step-size, and (iii) presence of local inaccuracy in images when inhomogeneous samples are scanned with a large step size. In addition, radiation damage is observed in some typology of materials when operations are performed with high intensity and strongly focused beams.

Full field-micro X-ray fluorescence (FF-MXRF) imaging is a promising alternative method that allows laterally resolved X-ray spectroscopy avoiding the scanning. The full area of a sample is illuminated with a broad primary beam inducing the emission of X-ray fluorescence by atomic species. The X-ray fluorescence is detected with a position-sensitive X-ray detector through a polycapillary (or a pinhole), properly positioned between the sample and detector (Figure 1a).

To date, few experimental approaches have been used for performing the FF-MXRF imaging. In 2012, a sophisticated pnCCD (the SLCam by pnSensor, IAP, BAM, and IFG) was developed and coupled to polycapillary optics.[18,19] This color X-ray camera (CXC), is a 264 × 264 array of silicon pixels with

Received: July 22, 2016
Accepted: September 22, 2016
Published: September 22, 2016

DOI: 10.1021/acs.analchem.6b02811
Anal. Chem. 2016, 88, 9873−9880

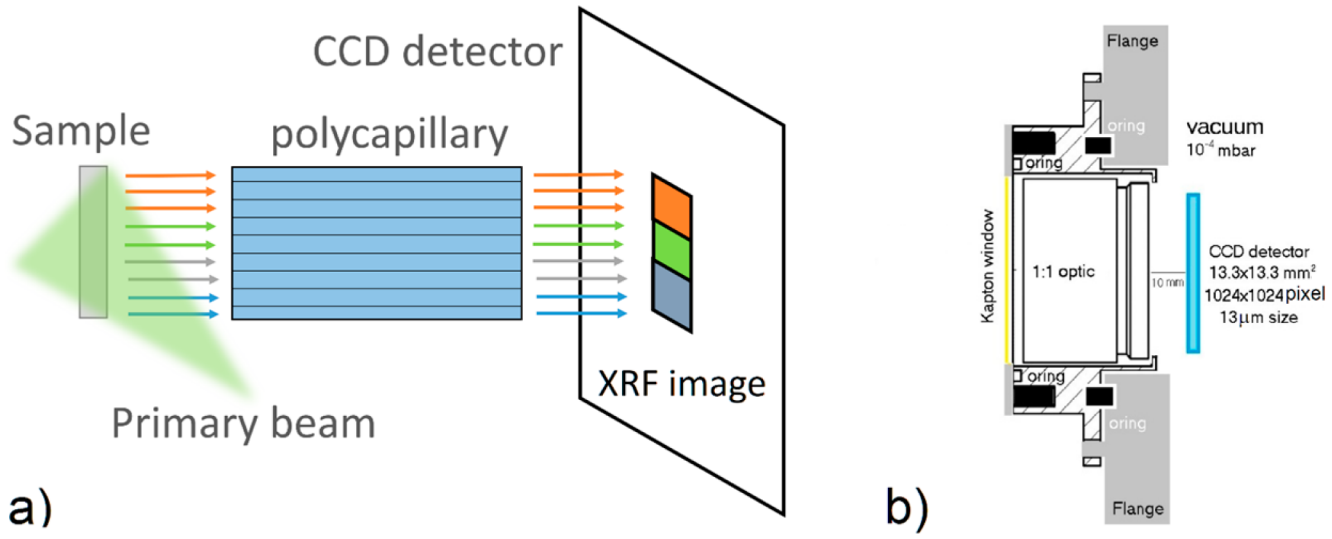

Figure 1. (a) Full Field Micro X-ray Fluorescence method with a 1:1 polycapillary. (b) A schematic view of the Full Field X-ray Camera.

a 48 μm lateral size and a 12 × 12 mm^2 active area. It works with a frame rate of 1 kHz.

Energy resolution of the CXC is <160 eV at 5.9 keV. The use of special 1:1 and 1:6 polycapillary optics allowed a spatial resolution of 50 and 5 μm, respectively.[18−21]

The CXC was successfully used in different applications both in laboratory and in synchrotron beamlines.[22−26] Very recently a new setup for in vacuum PIXE applications was installed as well.[20,27]

In 2014, it was demonstrated the feasibility of using a conventional MOS-CCD detector for performing the energy dispersive detection of fluorescence X-rays.[28,29] A deep cooling of the camera and the development of a special algorithm in a single photon counting technique allowed an energy resolution down to 133 eV at 5.9 keV. Other parameters affecting energy resolution of detector are read-out speed and binning size.[29]

A FF-XRF system was developed by coupling this CCD with pinhole collimators and by using a low power X-ray tube as primary X-ray source. Elemental maps were obtained with a lateral resolution of 25 μm at a 3× magnification. In addition, the possibility to operate a demagnification of samples, allowed operating the macro FF-XRF with a large field of view (50 × 50 mm^2) and a spatial resolution of 140 μm.[29] New updates have been recently introduced in this device aimed to develop a more efficient tabletop instrument.

The global efficiency of the system was improved by installing a 1:1 polycapillary instead of pinholes in front of the CCD. The original algorithm used for processing the events hitting the detector was optimized and adapted to work with faster shift register speeds (3 or 5 MHz) available in the detector with the result of an increased frame rate.

A new software with a graphical user interface (GUI) was programmed in Matlab. It fully controls the operating parameters of the device; it allows to perform on the fly the elemental imaging of samples with a region of interest (ROI) method. At the end of a measurement, it creates the spectra of each pixel allowing one to analyze collected data sets with a least-squares fitting imaging procedure available in external analytical tools (for instance in PyMCA).[30]

The low cost of the system, compact dimensions, and the easy-to-use electronics (only a USB cable and an office PC is necessary to control the instrument) make this device a valid tool for laboratory full field-X-ray fluorescence imaging applications. In this work its potentialities in both a FF-MXRF tabletop device and a FF-MPIXE end-station are investigated. Compelling applications in different scientific fields are presented and discussed as well.

EXPERIMENTAL SECTION

Full Field-X-ray Camera. The full field-X-ray camera (FF-XRC) consists of a conventional CCD detector (by Andor) equipped with a 1:1 polycapillary acting as an X-ray imaging optic. A schematic view of the FF-XRC is given in Figure 1b.

The CCD sensor is composed of 1024 × 1024 pixels with 13 μm lateral size and 40 μm thickness. The main technical capabilities of the detector (i.e., quantum efficiency, read-out speed, and binning capabilities) have been discussed in previous works.[28,29]

A straight shaped polycapillary (provided by IFG) was installed in front of the chip at about a 10 mm distance. The polycapillary optic presents a 25 mm diameter and 30 mm length. The capillary size is about 20 μm.

The optic is installed in a custom-built measurement head that is connected to the front flange of the CCD. Both detector and optic work in a 5 × 10^{-4} mbar vacuum during measurements. Air-vacuum interface is a 13 μm thick Kapton foil. In addition, a removable 25 μm thick Be window is installed in front of the CCD in order to block the visible radiation during the measurements.

A Peltier platform and an external water circulation at 20 °C keep the detector at a temperature of −95 °C. This allows a strong reduction in the electronic noise and improves the spectroscopic capabilities of the device.

The use of the FF-XRC as a high-resolution energy dispersive X-ray detector is based on a single photon counting (SPC) technique in a multiframe acquisition procedure.[29] In general, many thousands of SPC frames are necessary to obtain the statistics for the simultaneous elemental imaging of samples.

A processing algorithm was developed for correcting each SPC frame for the presence of a group of illuminated pixels (due both to single and multiple hitting events occurring in neighboring pixels of detector plane). This procedure allows one to determine the charge generated in each of the pixel by

DOI: 10.1021/acs.analchem.6b02811
Anal. Chem. 2016, 88, 9873−9880

incident X-rays and, thanks to a preliminary calibration with pure target materials, the energy of incident photons.

An energy resolution <155 eV at 5.9 keV was determined when the device is operated at the working parameters (chosen as default values) of −85 °C temperature, 1 MHz read-out speed, and a binning value of 4. Spatial resolution was measured by USAF1951 reference pattern irradiated at a distance of 10 mm from the polycapillary. As expected, the use of a polycapillary with a 20 μm capillary size and CCD binned at 4 (corresponding to a pixel size of 52 μm in the present detector) allowed one to obtain a lateral resolution of 55 μm.

The main limit in using a conventional CCD for energy dispersive measurement is frame rate. At the default parameters of 1 MHz read-out speed and 4 binning, it is 8 frames per second. Faster read-out speeds of 3 and 5 MHz are possible in detector. However, some considerations are needed for their proper use with the SPC technique adopted in the FF-XRC.

When a photon illuminates a single pixel, the relation between generated-charge and photon energy is maintained. In this case no intervention is necessary with respect to the use of the default 1 MHz read-out. Only a slight decrease of energy resolution is observed due to a higher read-out electronic noise.

On the contrary, a group of illuminated pixels generated by a single photon at 3 or 5 MHz present a large extension due to smearing effects arising from a faster reading of data. If SPC frames are not properly processed, the final X-ray spectrum could present tailing effects (or additional peaks) due to inaccuracies arising for an incomplete charge reconstruction.

The processing algorithm for the treatment of the SPC frames has been further optimized. The event reconstruction procedure is now operated by investigating presence of illuminated pixels in large regions of CCD; hypothetically the search of illuminated pixels belonging to a given group could extend to the full sensor instead of the limited number 25 × 25 pixels used in the previous version of the algorithm. Figure 2

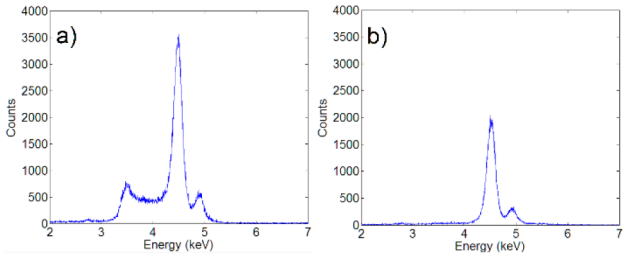

Figure 2. A Ti target measured at a read-out speed of 3 MHz and processed with (a) the previous version of the algorithm and (b) the new one.

shows a comparison of the measurement of a Ti target at 3 MHz by using the old (Figure 2a) and the new (Figure 2b) version of the processing algorithm, respectively. It is evident how the changes introduced in the processing procedure allow an excellent spectrum reconstruction.

The possibility of using the faster read-out speeds now allows one to operate with 15−20 frames per second. In addition, the use of higher binning values or the cropping of the CCD sensor can allow one to work up to 50 frames per second with the drawback to operate with a lower spatial resolution or with a lower field of view.

A new software with a graphical user interface (GUI) was programmed in Matlab. It is shown in Figure S1 of the Supporting Information.

It allows one to setup the acquisition parameters of the detector, to process in a live mode the SPC frames, and to apply a ROI imaging procedure to the X-ray line detected in the integral spectrum. The software works by using the *n*-dimensional sparse matrix approach for the zero suppression available in Matlab. This allows one to reduce the storage dimension of the large data set acquired in a single measurement.

At the end of the acquisition, the software determines the X-ray spectra of each pixel and allows the user to store them in different formats (i.e., CSV, EDF, HDF5). This way final data can be imported and analyzed with an external analytical tool allowing the elemental imaging based on a least-squares fitting procedure. Figure 3 shows an X-ray spectrum measured with the FF-XRC and fitted by PyMCA with proper configuration files.

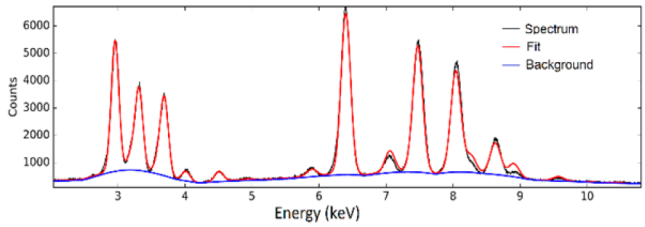

Figure 3. FF-XRC spectrum processed with the least-squares fitting module in PyMCA.

Tabletop FF-MXRF Device. The X-ray camera was installed in a table top full field-micro X-ray fluorescence setup based on a 3 kW power X-ray tube. The X-ray source is equipped with a Mo anode and allows one to operate with a maximum of 50 kV high voltage and 60 mA current. A schematic view of the FF-MXRF device is given in Figure 4.

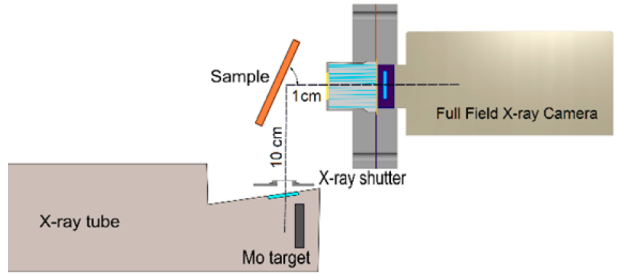

Figure 4. Schematic view of the tabletop FF-XRF instrument.

The distance between the source and the sample is 100 mm, and the incident angle of the primary X-ray beam with respect to sample surface can range between 20° and 45° for different irradiation setups. The X-ray beam is not collimated; its dimension at the sample position is 5 × 5 cm^2 that fully cover the field of view of the FF-XRC.

Sample is fixed in a sample holder at a distance of 10 mm from the front-window of the X-ray camera. The fine positioning is performed with two linear stages with a micrometric precision. In addition, a rotation stage is used for tilting the samples at the angle to be used during irradiation.

Finally, a programmable X-ray shutter is installed on the X-ray source and it is used to stop the X-ray beam during the readout process. This way the distortion and smearing effects on the images due to readout time are eliminated.

DOI: 10.1021/acs.analchem.6b02811
Anal. Chem. 2016, 88, 9873−9880

FF-MPIXE End Station. The FF-XRC camera was used for the first time in a FF-MPIXE end station operating with a low-energy proton beam of wide dimensions extracted in the air. The measurement station has been installed at the 80° beamline of the Laboratori Nazionali del Sud (LNS) of the Italian National Institute of Nuclear Physics (INFN). The experimental setup is illustrated in Figure 5a; Figure 5b shows a picture of the measurement station with indication of the main components.

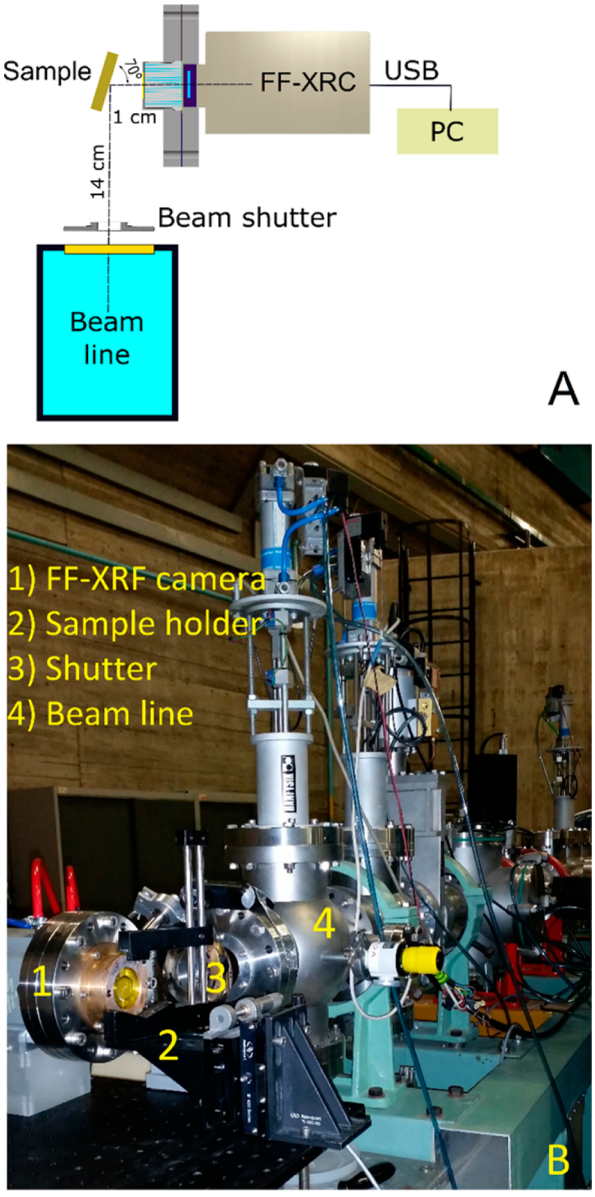

Figure 5. (a) Schematic view of the FF-MPIXE end station (b) and the experimental setup.

The beamline is served by a 13 MV TANDEM accelerator that provides, among others ions, proton beams up to 25 MeV energies. Proton energy can be tuned down to about 5 MeV and a maximum current of 1 μA can be delivered to users for experiments. A proton beam of 6 MeV energy was extracted in air by using a 100 μm Kapton window as a vacuum−air interface.

An electronic shutter is positioned between the exit window of the beamline and the sample. It works as a beam stopper with an open/close time of 15 ms. The shutter trigger is given by the control software of the FF-XRC during the read-out process.

A sample holder equipped with a 4 axis travel system (i.e., 3 linear stages each one allowing a 25 mm travel in the *XYZ* directions, respectively, and 1 rotation stage for the sample tilting) was positioned at about 14 cm from the Kapton window. This air path allows to degrade proton energy down to a value of about 3 MeV, better suited for performing PIXE measurements on samples. Energy straggling is only 120 keV as estimated by the SRIM (formerly TRIM) Monte Carlo simulation code (Figure 6a).

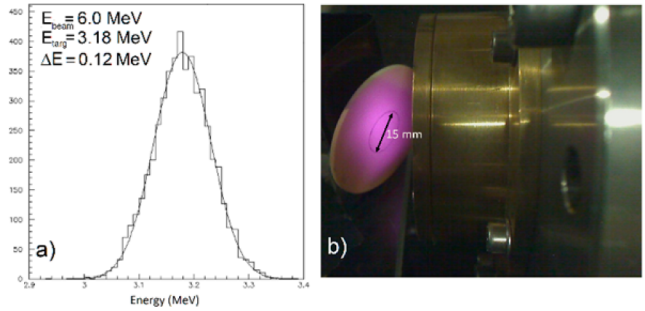

Figure 6. Energy and straggling of proton beam evaluated by a SRIM simulation (a) and beam dimension at the sample position (b).

The full field-X-ray camera is positioned in a 90° geometry with reference to the beam direction. Samples to be investigated are tilted of an angle of 20° and they are placed at 10 mm distance from the detector. Figure 6b shows the beam dimensions during the irradiation of an alumina target at the sample positon in front of the FF-XRC.

The beam dimension is about 30 mm diameter that fully cover the field of view of the detector. Such a large beam diameter is obtained by strongly focusing the beam inside the beamline and taking advantage of its divergence at the measurement distance.

RESULTS AND DISCUSSION

FF-MXRF Imaging. The FF-MXRF tabletop device was used for simultaneous nondestructive mapping of the atomic species in biological and geological/archeological materials. In particular, potentialities of the FF-MXRF methodology have been verified in measurements concerning the elemental imaging of a bee body.

This measurement is particularly significant since it shows how FF-MXRF overcomes limits of conventional scanning MXRF in the case of nonflat samples. Moreover, analysis is nondestructive and no sample preparation is required. The trace elements in the tissues of bees were determined in previous works with the aim of studying effects of the environment on bee health and reproduction and for determining the quality of the honey production.[31]

It was demonstrated by different analytical techniques (i.e., TXRF, AES, ICP-MS) that trace elements in the bee tissues are connected to environmental pollution. In addition, they can be used for controlling the quality of honey in the area were bees live. Analytical techniques used in previous works are destructive and required a complex procedure for sample

DOI: 10.1021/acs.analchem.6b02811
Anal. Chem. 2016, 88, 9873−9880

preparation. Table S1 of Supporting Information summarizes compositional data of trace elements published in the literature.[31]

A bee body was investigated with FF-MXRF. It was irradiated for 6700 s (500 ms exposure time per frame and 172 ms readout time per frame) with the X-ray source operated at 35 kV and 20 mA. Measurements were performed by using the CCD at a binning value of 4 and a readout speed of 1 MHz.

The X-ray spectrum obtained during the measurement is shown in Figure S2 of the Supporting Information. It shows elements contained at the trace level in the bee tissues (i.e., K, Ca, Mn, Fe, Cu, and Zn).[31] Contaminations due to the sample holder (a steel-brass needle) are visible as well. Figure 7 shows the elemental maps obtained during the FF-MXRF measurement.

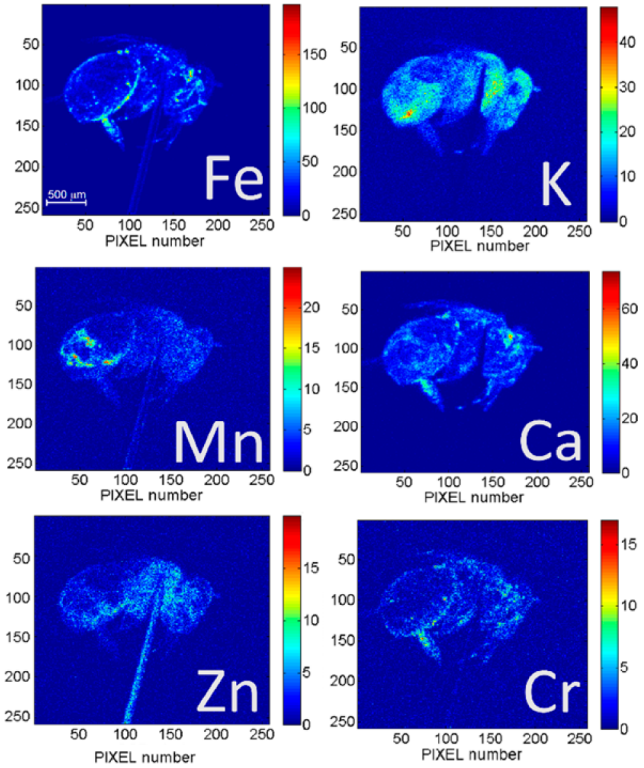

Figure 7. Elemental maps of the bee obtained by the FF-MXRF tabletop device.

The images were obtained by applying the least-squares fitting procedure available in PyMCa on the experimental data exported in a EDF format by the FF-XRC software. The spectroscopic capabilities of the FF-MXRF allowed one to distinguish with high accuracy the K-lines of the main chemical elements. In the case of Zn, the contamination due to the needle used as the sample holder is also visible.

Figure 8 shows the elemental maps of Fe and Mn taken by tilting the sample in order to irradiate the back side. This approach allows in some analytical cases to better resolve the distribution of chemical elements in a three-dimensional sample. However, it should be noted that since the technique provides information integrated along the depth of the field of the X-ray camera, some inaccuracies could arise in the final elemental distribution.

The second application of the FF-MXRF concerns the analysis of Lapis lazuli stones. Lapis lazuli is one of the most

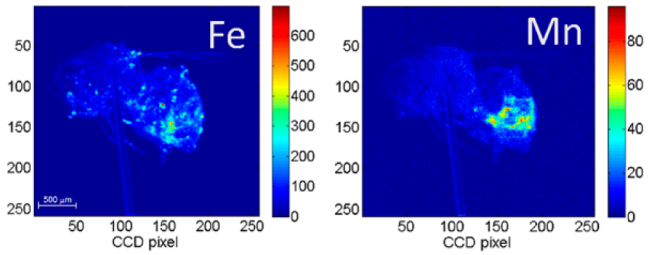

Figure 8. Elemental map of Fe and Mn taken with sample tilted on the back side.

ancient stones used in antiquity as a precious decoration of objects. From the geochemical point of view, Lapis lazuli is composed by the Lazurite mineral $Na_3Ca(Si_3Al_3O_{12})S$ with other inclusions like Calcite, Diopside, Wollastonite, and Pyrite.

Procurement of Lapis lazuli in ancient time has been identified in the sources located in Afghanistan. Despite other sources of Lapis lazuli being known (Siberia, Pamir, Myanmar, etc.), it is not well-established if and at what extent these sources have been exploited. Consequently, determination of the provenance of ancient Lapis lazuli is a question of both geological and archeological interest that has pushed development of different analytical approaches.[32]

FF-MXRF was used to map the chemical elements of a Lapis lazuli from Siberia. Results are summarized in Figure 9.

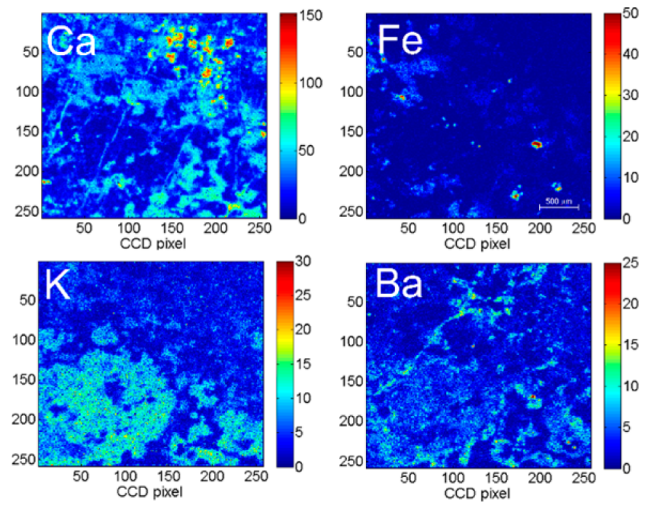

Figure 9. Elemental maps of a Lapis lazuli from Siberia.

Measurements were performed by using the detector at a binning value of 4 and a readout speed of 1 MHz. The X-ray source was operated at 40 kV and 20 mA. The total measurement time was 2700 s, and the total number of frames were 10 000 with 270 ms time (including both exposure and read-out times) per frame. It is evident that FF-MXRF provides information on the main expected components of the precious stone.

The pattern of Ca-rich and K-rich phases, detected with high lateral resolution, together with the presence of traces of Ba and inclusions of Fe (Pyrite) constitute a fingerprint for the Siberia source.[30] More in general, results evidenced how FF-MXRF can be a nondestructive analytical tool to be used in provenance studies in comparison with data obtained from materials coming from other known and unknown sources.[32]

DOI: 10.1021/acs.analchem.6b02811
Anal. Chem. 2016, 88, 9873−9880

FF-MPIXE Imaging. Particle induced X-ray emission (PIXE) allows measurements of fluorescence K lines of low Z elements with higher ionization cross section. Moreover, because of the high stopping power of charged particles in the matter, the analytical depth of PIXE is well-defined and limited to the near surface layer. Finally, accelerated charge particle beams can be tuned in energy and a differential PIXE can be applied for an in-depth compositional integrated profile of samples.[33]

In this section it is demonstrated the feasibility of the FF-MPIXE imaging in analytical applications based on the use of a wide dimension proton beam extracted in air. Samples discussed in this section consist of (i) a fragment of a polychrome pottery belonging to the Nasca culture from Peru (Figure 10) dating to the fifth century AD; (ii) a late Roman silvered *nummus* belonging to the Treasure of Misurata (Lybia) dated back to 330−333 AD (Figure 11).

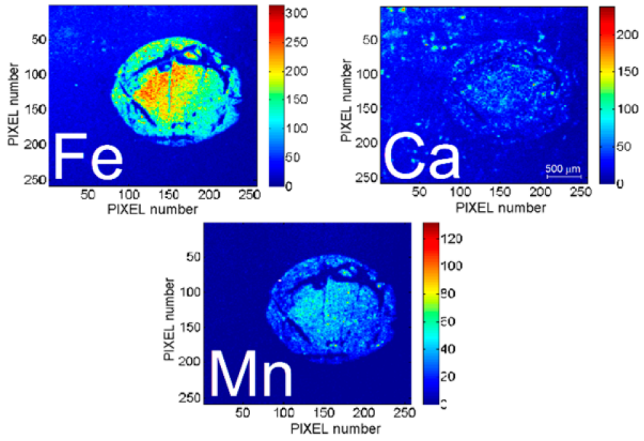

Figure 10. Nasca sample and the elemental maps obtained by the FF-MPIXE technique.

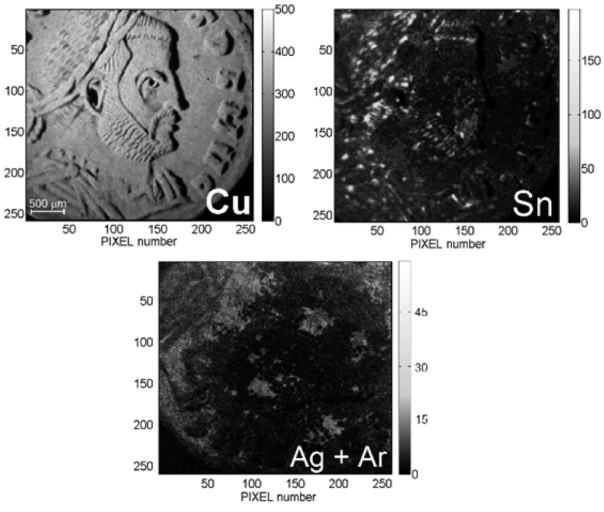

Figure 11. Silvered *nummus* investigated with the FF-MPIXE technique.

Measurements of the samples were performed by using the FF-XRC at a binning value of 4 and a readout speed of 1 MHz. Samples were irradiated for about 5 h with a proton current of 30 nA. The energy of protons in the sample position was about 3 MeV. Figure 10 shows the FF-MPIXE elemental maps of the decorative layer in the surface of the painted pottery.

The main chemical components of the black decoration are Mn and Fe, as expected for the case of a manganese-black technique. In addition, the elemental maps show the presence of Ca with a coarse distribution and with an enriched presence in correspondence of the black decoration. This suggest the association of Ca to the clay materials used for manufacturing the slip in the black decoration layer as verified by authors in a previous work with different analytical techniques.[34]

A comparison between the FF-MPIXE and FF-MXRF results on the same sample is given in Figure S3 of the Supporting Information in order to evidence the potentiality of FF-MPIXE in exciting the light elements.

The second application investigated by the FF-MPIXE concerns a late Roman *nummus* dated back to 330−333 AD. The surface silvering of coins was adopted as a common practice during late Roman empire for giving the impression of a higher finesses despite a global debasement of the alloy. The *nummus*, introduced by Diocletian in 294 AD, is manufactured with a quaternary alloy (Cu−Sn−Pb-Ag) with a 1−2 μm thickness silvered patina on the surface.

Different analytical approaches have been developed in the past for investigating the composition of both the patina and bulk and to determine the manufacturing technology of the Ag-plated surface of the Roman *nummi*.[35−37]

FF-MPIXE imaging is particularly suited for the characterization of archeological metals. The determination of the elemental distribution can support metallurgical studies devoted to gain new information on manufacturing technology and conservation states. Figure 11 shows the FF-MPIXE elemental imaging of the Roman *nummus*.

Copper is the main constituent of the alloy. Its distribution appears homogeneous in the surface layer investigated with protons. Previous works evidenced that total weight concentration of copper is around 90−95%.[35−37]

On the contrary, Sn presents an in homogeneous distribution. This spotted distribution suggests an incomplete solution of tin in quaternary alloy and, consequently, a limit of the metallurgical process used for the *nummus* coinage. This results evidence the limit of compositional studies often performed in archeological metals with local or punctual measurements.

Finally, Ag map was determined by using the Ag-L lines at 2.957 keV. Because of the large self-absorption, the use of L-lines of Ag allows to limit the investigation mainly to the patina covering the surface of the coin. It is evident that the silvered patina is strongly degraded due to the circulation and the burial. However, Ag L-lines are partially overlapped in the spectra with the Ar K-lines from the air. Consequently, images are particularly noisy and they can present some local inaccuracies.

CONCLUSIONS

A full field-X-ray camera presenting high-energy and high-spatial resolution was developed with the aim to perform the elemental mapping of samples in micro-XRF and micro-PIXE imaging spectroscopy. The FF-XRC consists of a conventional CCD detector equipped with a straight shaped polycapillary that works as a 1:1 imaging optic. The FF-XRC is fully controlled with an in-house programmed software working with a GUI in a Matlab environment.

A multiframe acquisition with a single-photon counting technique enabled the use of the CCD detector as an energy

DOI: 10.1021/acs.analchem.6b02811
Anal. Chem. 2016, 88, 9873−9880

dispersive detector. A custom-developed algorithm is used to process each frame and to determine the X-ray spectra in each pixel in the CCD sensor.

A ROI-based imaging can be applied in a live mode during the measurement. At the end of the acquisition, the full data set can be exported in different formats (i.e., CSV, EDF, HDF5) and analyzed with external analytical tools (e.g., PyMCA) that allows imaging procedures with a least-squares fitting of data. This way artifacts in elemental images that can occur by the use of ROI method are minimized or eliminated.

Energy resolution of the device is about 150 eV at 5.9 keV and spatial resolution down to 50 μm at the CCD working parameters of −85 °C cooling temperature, 1 MHz read-out speed, and 4 binning value. The FF-XRC operated at these parameters allows the acquisition of 8 frames per seconds. A further optimization of the processing algorithm allowed the use of faster read-out speeds. A frame-rate up to 50 was obtained with a slight reduction of the energy resolution of the FF-XRC.

The FF-XRC was tested with different analytical techniques. First, a tabletop FF-XRF device operating with a high brilliance Mo-target X-ray tube was installed and used for the full field-micro X-ray fluorescence of samples of biological and geological/archeological interest.

Finally, the feasibility of using the X-ray camera in a PIXE setup was verified. A FF-MPIXE end station was installed at the INFN-LNS laboratory and used with a 3 MeV energy proton beam accelerated by a 13 MV TANDEM accelerator and extracted in air. The proton beam was unfocused to a 3 cm diameter and successfully used for the PIXE microimaging of samples of interest in the cultural heritage field.

■ ASSOCIATED CONTENT

Supporting Information

The Supporting Information is available free of charge on the ACS Publications website at DOI: 10.1021/acs.analchem.6b02811.

GUI of the new control software of the FF-XRC, X-ray spectrum obtained from the FF-MXRF measurement of a bee, comparison of FF-MPIXE and FF-MXRF measurements on the Nasca pottery of Figure 10, and trace element contents obtained with TXRF, AAS, and ICP-AES for bee tissues (PDF)

■ AUTHOR INFORMATION

Corresponding Author

*E-mail: romanop@lns.infn.it.

Notes

The authors declare no competing financial interest.

■ ACKNOWLEDGMENTS

The research of the present paper was performed at the LANDIS laboratory of Catania (Italy) in the framework of a scientific cooperation between INFN-LNS and IBAM-CNR. This research is included in the activities of the CHNET Network of the INFN. Funding support for the research was given by the Fifth National Committee of INFN.

■ REFERENCES

(1) Haschke, M. *Laboratory Micro-X-Ray Fluorescence Spectroscopy*, 1st ed.; Springer: London, U.K., 2014.

(2) Janssens, K. H. A.; Adams, F. C. V.; Rindby, A. *Microscopic X-Ray Fluorescence Analysis*; Wiley: Chichester, U.K., 2002.

(3) Bjeoumikhov, A.; Bjeoumikhova, S.; Wedell, R. *Part. Part. Syst. Charact.* **2009**, *26*, 97−106.

(4) Schroer, C. G.; Boye, P.; Feldkamp, J. M.; Patommel, J.; Samberg, D.; Schropp, A.; Schwab, A.; Stephan, S.; Falkenberg, G.; Wellenreuther, G.; Reimers, N. *Nucl. Instrum. Methods Phys. Res., Sect. A* **2010**, *616*, 93−97.

(5) Kanngießer, B.; Malzer, W.; Mantouvalou, I.; Sokaras, D.; Karydas, A. G. *Appl. Phys. A: Mater. Sci. Process.* **2012**, *106*, 325−338.

(6) Giuntini, L.; Massi, M.; Calusi, L. *Nucl. Instrum. Methods Phys. Res., Sect. A* **2007**, *576*, 266−273.

(7) Ryan, C. G. *Nucl. Instrum. Methods Phys. Res., Sect. B* **2011**, *269*, 2151−2162.

(8) Pichon, L.; Calligaro, T.; Lemasson, Q.; Moignard, B.; Pacheco, C. *Nucl. Instrum. Methods Phys. Res., Sect. B* **2015**, *363*, 48−54.

(9) Karydas, A. G.; Sokaras, D.; Zarkadas, C.; Grlj, N.; Pelicon, P.; Žitnik, M.; Schütz, R.; Malzer, W.; Kanngießer, B. *J. Anal. At. Spectrom.* **2007**, *22*, 1260−1265.

(10) Nakano, K.; Nishi, C.; Otsuki, K.; Nishiwaki, Y.; Tsuji, K. *Anal. Chem.* **2011**, *83*, 3477−3483.

(11) Mihucz, V. G.; Meirer, F.; Polgári, Z.; Réti, A.; Pepponi, G.; Ingerle, D.; Szoboszlai, N.; Streli, C. *JBIC, J. Biol. Inorg. Chem.* **2016**, *21*, 241−249.

(12) Vogel-Mikus, K.; Pongrac, P.; Pelicon, P. *Int. J. PIXE* **2014**, *24*, 217−233.

(13) Santos, H. C.; Caliri, C.; Pappalardo, L.; Catalano, R.; Orlando, A.; Rizzo, F.; Romano, F. P. *Microchem. J.* **2016**, *124*, 241−246.

(14) Janssens, K.; Van Der Snickt, G.; Alfeld, M.; Noble, P.; van Loon, A.; Delaney, J.; Conover, D.; Zeibel, J.; Dik, J. *Microchem. J.* **2016**, *126*, 515−523.

(15) Egerton, V. M.; Wogelius, R. A.; Norell, M. A.; Edwards, N. P.; Sellers, W. I.; Bergmann, U.; Sokaras, D.; Alonso-Mori, R.; Ignatyev, K.; van Veelen, A.; Anné, J.; van Dongen, B.; Knoll, G.; Manning, P. L. *J. Anal. At. Spectrom.* **2015**, *30*, 627−634.

(16) Uhlir, K.; Padilla-Alvarez, R.; Migliori, A.; Karydas, A. G.; Božičević Mihalić, I.; Jakšić, M.; Zamboni, I.; Lehmann, R.; Stelter, M.; Griesser, M.; Schindel, N.; Alram, M. *Microchem. J.* **2016**, *125*, 159−169.

(17) Lühl, L.; Mantouvalou, I.; Schaumann, I.; Vogt, C.; Kanngießer, B. *Anal. Chem.* **2013**, *85*, 3682−3689.

(18) Scharf, O.; Ihle, S.; Ordavo, I.; Arkadiev, V.; Bjeoumikhov, A.; Bjeoumikhova, S.; Buzanich, G.; Gubzhokov, R.; Gunther, A.; Hartmann, R.; Kuhbacher, M.; Lang, X. M.; Langhoff, N.; Liebel, A.; Radtke, M.; Reinholz, U.; Riesemeier, H.; Soltau, H.; Struder, L.; Thunemann, A. F.; Wedell, R. *Anal. Chem.* **2011**, *83*, 2532−2538.

(19) Ordavo, I.; Ihle, S.; Arkadiev, V.; Scharf, O.; Soltau, H.; Bjeoumikhov, A.; Bjeoumikhova, S.; Buzanich, G.; Gubzhokov, R.; Gunther, A.; Hartmann, R.; Holl, P.; Kimmel, N.; Kuhbacher, M.; Lang, M.; Langhoff, N.; Liebel, A.; Radtke, M.; Reinholz, U.; Riesemeier, H.; Schaller, G.; Schopper, F.; Struder, L.; Thamm, C.; Wedell, R. *Nucl. Instrum. Methods Phys. Res., Sect. A* **2011**, *654*, 250.

(20) Nowak, S. H.; Bjeoumikhov, A.; von Borany, J.; Buchriegler, J.; Munnik, F.; Petric, M.; Renno, A. D.; Radtke, M.; Reinholz, U.; Scharf, O.; Strüder, L.; Wedell, R.; Ziegenrücker, R. *X-Ray Spectrom.* **2015**, *44*, 135−140.

(21) Nowak, S. H.; Bjeoumikhov, A.; von Borany, J.; Buchriegler, J.; Munnik, F.; Petric, M.; Radtke, M.; Renno, A. D.; Reinholz, U.; Scharf, O.; Wedellg, R. *J. Anal. At. Spectrom.* **2015**, *30*, 1890−1897.

(22) Kühn, A.; Scharf, O.; Ordavo, I.; Riesemeier, H.; Reinholz, U.; Radtke, M.; Berger, A.; Ostermann, M.; Panne, U. *J. Anal. At. Spectrom.* **2011**, *26*, 1986−1989.

(23) Reiche, I.; Müller, K.; Albéric, M.; Scharf, O.; Wähning, A.; Bjeoumikhov, A.; Radtke, M.; Simon, R. *Anal. Chem.* **2013**, *85*, 5857−5866.

(24) Radtke, M.; Buzanich, G.; Curado, J.; Reinholz, U.; Riesemeier, H.; Scharf, O. *J. Anal. At. Spectrom.* **2014**, *29*, 1339−1344.

DOI: 10.1021/acs.analchem.6b02811
Anal. Chem. 2016, 88, 9873−9880

(25) Fittschen, U. E. A.; Menzel, M.; Scharf, O.; Radtke, M.; Reinholz, U.; Buzanich, G.; Lopez, V. M.; McIntosh, K.; Streli, C.; Havrilla, G. J. *Spectrochim. Acta, Part B* **2014**, *99*, 179−184.
(26) Radtke, M.; Buzanich, G.; Guilherme, A.; Reinholz, U.; Riesemeier, H.; Scharf, O.; Scholz, P.; Guerra, M. F. *Microchem. J.* **2016**, *125*, 56−61.
(27) Hanf, D.; Buchriegler, J.; Renno, A. D.; Merchel, S.; Munnik, F.; Ziegenrücker, R.; Scharf, O.; Nowak, S. H.; von Borany, J. *Nucl. Instrum. Methods Phys. Res., Sect. B* **2016**, *377*, 17−24.
(28) Romano, F. P.; Altana, C.; Cosentino, L.; Celona, L.; Gammino, S.; Mascali, D.; Pappalardo, L.; Rizzo, F. *Spectrochim. Acta, Part B* **2013**, *86*, 60−65.
(29) Romano, F. P.; Caliri, C.; Cosentino, L.; Gammino, S.; Giuntini, L.; Mascali, D.; Neri, L.; Pappalardo, L.; Rizzo, F.; Taccetti, F. *Anal. Chem.* **2014**, *86*, 10892−10899.
(30) Solé, V. A.; Papillon, E.; Cotte, M.; Walter, Ph.; Susini, J. *Spectrochim. Acta, Part B* **2007**, *62*, 63−68.
(31) Kump, P.; Necemer, M.; Snajder, J. *Spectrochim. Acta, Part B* **1996**, *51*, 499−507.
(32) Calligaro, T.; Coquinot, Y.; Pichon, L.; Pierrat-Bonnefois, G.; de Campos, P.; Re, A.; Angelici, D. *Nucl. Instrum. Methods Phys. Res., Sect. B* **2014**, *318*, 139−144.
(33) Mandò, P. A.; Fedi, M. E.; Grassi, N. *Eur. Phys. J. Plus* **2011**, *126*, 41−50.
(34) Romano, F. P.; Pappalardo, L.; Masini, N.; Pappalardo, G.; Rizzo, F. *Microchem. J.* **2011**, *99*, 449−453.
(35) Romano, F. P.; Garraffo, S.; Pappalardo, L.; Rizzo, F. *Spectrochim. Acta, Part B* **2012**, *73*, 13−19.
(36) Rizzo, F.; Cirrone, G. P.; Cuttone, G.; Esposito, A.; Garraffo, S.; Pappalardo, G.; Pappalardo, L.; Romano, F. P.; Russo, S. *Microchem. J.* **2011**, *97*, 286−290.
(37) Pappalardo, L.; Alberti, R.; Calì, C.; Garraffo, S.; Litrico, P.; Pappalardo, G.; Rizzo, F.; Romano, F. P. *X-Ray Spectrom.* **2013**, *42*, 33−37.

DOI: 10.1021/acs.analchem.6b02811
Anal. Chem. 2016, 88, 9873−9880